Journal of the Korean Physical Society (2022) 81:278–284
https://doi.org/10.1007/s40042-022-00521-y

Online ISSN 1976-8524
Print ISSN 0374-4884

ORIGINAL PAPER - CROSS-DISCIPLINARY PHYSICS AND RELATED AREAS OF SCIENCE AND TECHNOLOGY

Structural and optical characteristics of antimony selenosulfide thin films prepared by two-step method

Fulya Turkoglu[1,2] · Memduh Emirhan Ekren[1] · Ayten Cantas[3] · Kubra Yakinci[4] · Hazal Gundogan[5] · Hasan Koseoglu[2] · Gulnur Aygun[5] · Lutfi Ozyuzer[5,6]

Received: 18 April 2022 / Revised: 11 May 2022 / Accepted: 19 May 2022 / Published online: 4 July 2022

Abstract

Antimony triselenide (Sb_2Se_3) is one of the most promising absorber material choices among the inorganic semiconductors that has attracted much attention today. However, highest recorded efficiencies for Sb_2Se_3 solar cells are still lower than ideal. Exploring antimony selenosulfide ($Sb_2(S_xSe_{1-x})_3$) to increase device performance is one option because some features of alloyed $Sb_2(S_xSe_{1-x})_3$ depend on composition such as bandgap and band position. In this study, two-step process was used to grow $Sb_2(S_xSe_{1-x})_3$ thin films. In the first stage, Sb_2Se_3 thin films were deposited on soda lime glass substrates using direct current magnetron sputtering technique. In the second stage, Sb_2Se_3 thin films were exposed to sulfurization process in a quartz ampoule to obtain $Sb_2(S_xSe_{1-x})_3$ thin films. Characterization results showed that morphological, optical, and structural properties of $Sb_2(S_xSe_{1-x})_3$ thin films grown by presented method were highly dependent on amount of sulfur in the films. By the adjustment of the S/S + Se atomic ratio, $Sb_2(S_xSe_{1-x})_3$ absorber materials with suitable bandgap, favorable orientation and compact morphology can be obtained for photovoltaic applications.

Keywords Antimony selenosulfide · Magnetron sputtering · Thin film solar cells

1 Introduction

Inorganic compound thin-film solar cells have received considerable attention in the research community because of their features such as flexibility, minimal material and energy consumption. Among them, $Cu(In,Ga)Se_2$ (CIGS) and CdTe are the two most common thin-film photovoltaic materials having power conversion efficiencies (PCE) of over 22% [1, 2]. However, due to the high cost of In and Ga as well as the toxicity of Cd, cost effective thin-film solar cells are urgently needed. Alternatively, $Cu_2ZnSn(S,Se)_4$ (CZTSSe) thin films, which contain earth abundant and low-cost elements, could also be used in photovoltaic (PV) systems [3, 4]. However, it is difficult to obtain thin-film PV devices with high efficiency from $Cu_2ZnSn(S,Se)_4$ (CZTSSe) absorbers since photogenerated charge carriers undergo intense recombination in a variety of ways, resulting in a short minority carrier lifetime and diffusion length [5–7]. Antimony triselenide (Sb_2Se_3), which is one of the most promising absorber material choices among the inorganic semiconductors, can provide solutions to these limitations. Besides having nontoxic, earth abundant and low-cost elements, it has a proper bandgap (1.0–1.2 eV) and high optical absorption coefficient ($> 10^5$ cm^{-1}) allowing high optical absorption between visible and near-infrared (VIS/NIR) light region [8]. It has been demonstrated that photons having wavelengths higher than 800 nm can be entirely absorbed in the first 400 nm of the

✉ Fulya Turkoglu
fulya.koseoglu@iste.edu.tr

1 Department of Metallurgical and Materials Engineering, Iskenderun Technical University, 31200 Iskenderun, Hatay, Turkey

2 ISTE Center for Science and Technology Studies and Research (ISTE-CSTSR), Iskenderun Technical University, 31200 Iskenderun, Hatay, Turkey

3 Department of Electric and Energy, Pamukkale University, 20160 Kınıklı, Denizli, Turkey

4 Department of Engineering Basic Science, Iskenderun Technical University, 31200 Iskenderun, Hatay, Turkey

5 Department of Physics, Izmir Institute of Technology, 35430 Urla, Izmir, Turkey

6 Teknoma Technological Materials Ltd. IZTEKGEB, IZTECH Campus, 35430 Urla, Izmir, Turkey

Sb_2Se_3 film, allowing for significantly thinner absorber layers than in conventional thin-film solar cells [9]. The highest recorded efficiencies for Sb_2Se_3 solar cells have reached to 7.6% [10] and 9.2% [11]. Despite these endeavors, the performance of the current champion Sb_2Se_3 device is far from ideal represented by Shockley–Queisser model [12]. Therefore, to make Sb_2Se_3 solar cells more competitive, considerable research is required. Exploring $Sb_2(S_xSe_{1-x})_3$ to increase device performance is one option because some features of alloyed $Sb_2(S_xSe_{1-x})_3$ depend on composition such as bandgap and band position [13–15]. In a short period of time, the efficiency of the $Sb_2(S_xSe_{1-x})_3$ thin-film PV have already reached to 10.5% [16]. Due to the similar crystal structure of Sb_2Se_3 and Sb_2S_3 and the close ionic radius of sulfur and selenium, $Sb_2(S_xSe_{1-x})_3$ can be called a quasi-binary compound because sulfur and selenium can be alloyed in a continuous ratio [17, 18]. According to the Shockley–Queisser model, the theoretical energy conversion efficiency of a single junction solar cell is 33.7% for a semiconductor with optimum bandgap of 1.34 eV [12, 19]. Therefore, $Sb_2(S_xSe_{1-x})_3$ can be employed as an absorber with a better bandgap than Sb_2Se_3. Moreover, tuning the band position by changing composition of $Sb_2(S_xSe_{1-x})_3$ enables optimal band alignme nt between the buffer layer and absorber layer [15].

Appropriate absorber material processing is crucial to get solar cells with high efficiency because it affects morphological, structural, electrical as well as the defect properties of the materials in a PV device. In this regard, for the fabrication of state-of-the-art $Sb_2(S_xSe_{1-x})_3$ thin films, both vapor and solution-based deposition methods have been established [14, 20, 21]. Typically, $Sb_2(S_xSe_{1-x})_3$ thin films can be fabricated using a spin coating method, provided that the S, Se and Sb precursor components are dissolved in an appropriate solvent [13, 22]. However, films produced by this one-step method suffer from poor morphology with abundant pinholes formed in the films, which increases resistance of charge transfer and recombination probability of carriers. As a result, efficiency of the fabricated solar cell is approximately 7% [23]. Two-step method based on the post-selenization of grown Sb_2S_3 thin films, on the other hand, can produce uniform surface morphology [24, 25]. $Sb_2(S_xSe_{1-x})_3$ devices fabricated by two-step method has been demonstrated an efficiency of 7.82% [26]. In the studies mentioned above [24–26], Sb_2S_3 films was synthesized by wet chemical methods, namely chemical bath deposition (CBD) and hydrothermal method (HD). With such production methods, a lot of chemical waste is generated. It is clearly desirable to develop a green and simple two-step process for synthesizing $Sb_2(S_xSe_{1-x})_3$ thin films to avoid environmental pollution.

To the best of our knowledge, the preparation and characterization of $Sb_2(S_xSe_{1-x})_3$ thin films via sulfurization of preformed Sb_2Se_3 thin films in a quartz ampoule have not been studied yet. In this work, a series of $Sb_2(S_xSe_{1-x})_3$ thin films with $x = 0$, 0.12, 0.35, 0.48 and 0.86 were fabricated by the sulfurization of magnetron sputtered Sb_2Se_3 thin films in a quartz ampoule. The magnetron sputtering technique, which is a type of physical vapor deposition (PVD), has some advantages compared to the other methods such as high homogeneity in the produced films, good adhesion to substrates, possibility of depositing in large areas, high film growth rate and ability to easily control of the film thickness [27, 28]. For the sulfurization of thin films, it is a suitable method to place sulfur and thin film in a quartz ampoule, seal them under vacuum, and then apply heat treatment. In this way, toxic gases released during the sulfurization are prevented from spreading into the air. To sum up, in this study, it was aimed to investigate the morphological, optical, and structural properties of $Sb_2(S_xSe_{1-x})_3$ thin films grown by green and simple two-step process for PV applications.

2 Experimental

2.1 Sample preparation

In this work, two-step process was used to fabricate $Sb_2(S_xSe_{1-x})_3$ absorber layers. First, Sb_2Se_3 films were grown on soda lime glass (SLG) substrates by direct current (DC) magnetron sputtering technique using 2-in. target of Sb_2Se_3 (99.999%) at room temperature. Chamber was evacuated to a base pressure of 4.5×10^{-6} Torr by turbo molecular pump (TMP). After the chamber was backfilled with argon to a pressure of 1.2×10^{-3} Torr, pre-sputtering was performed for 5 min to remove the contamination of the surfaces of the Sb_2Se_3 target. Then, shutters were opened and the deposition of Sb_2Se_3 film on to the SLG continues 10 min to get Sb_2Se_3 films with 408 nm thickness. 30 standard cubic centimeter per minute (sccm) Ar was used as sputtering gas and the deposition was performed at 20 W. Substrate distance from the target surface was fixed at 8 cm for all depositions. In the second stage, Sb_2Se_3 thin films were exposed to sulfurization process in a quartz ampoule to obtain $Sb_2(S_xSe_{1-x})_3$ thin films. After sulfur (S) powder was poured into the one side of a quartz ampoule, necking was made at the middle of the quartz ampoule using O_2 flame. Then, fabricated Sb_2Se_3 films were placed on the other side of the quartz ampoule. Amount of S powder was changed between 1 and 4 mg to get $Sb_2(S_xSe_{1-x})_3$ films with different S/S + Se ratios. The volume of the used quartz ampoule was ≈ 16 ml with the inside diameter of 1.0 cm and length of 20 cm. The ampoule was evacuated to ≈ 1.2×10^{-2} mbar vacuum level using rough pump. After sealing was performed using O_2 flame, sealed quartz ampoule was placed into a furnace. Temperature ramping rate was kept constant as 25 °C per minutes for each sample and a temperature was

maintained at 350 °C for 30 min. Due to the low evaporation temperature of S, an intense sulfur vapor was formed in the quartz ampoule during the heat treatment and the film surface was homogeneously covered with sulfur. Finally, the ampoule was cooled naturally to RT and taken out from the furnace.

2.2 Characterization methods

The thickness of grown Sb_2Se_3 thin films was measured as 408 nm with A Veeco DEKTAK 150 profilometer. XRD was carried out to obtain information about crystal structures of the $Sb_2(S,Se)_3$ films. The XRD was operated in the Bragg–Brentano focusing geometry on a Malvern Panalytical Empyrean X-Ray diffractometry with Cu Kα radiation ($\lambda = 1.5406$ Å). XRD patterns were recorded from $2\theta = 10°–60°$ with step size of 0.013° and a time step of 33 s for all samples. The microstructural characterization of $Sb_2(S_xSe_{1-x})_3$ films was done using a high-resolution confocal micro-Raman spectroscopy (S&I, MonoVista, employing a Princeton Instruments, Acton SP2750 0.750 m Imaging Triple Grating Monochromator) in the back-scattering geometry with a spectral resolution of about 1 cm^{-1} at room temperature. Ar laser operating at 514.0 nm was used as the Raman excitation source. A 100 × objective giving spot sizes near 3 µm in diameter was employed to probe the vibrational modes of the $Sb_2(S_xSe_{1-x})_3$ films. SEM analysis was performed to examine the surface morphology of the $Sb_2(S_xSe_{1-x})_3$ compounds and EDS analysis was performed to determine their stoichiometry using the Thermo Fisher Scientific Apreo S LoVac SEM device equipped with UltraDry EDS Detector. Surface topography of the films was investigated by Everhart–Thornley detector (ETD) and T1 in-lens detector (Trinity Detection System) at 50,000 × magnification using 5–10 kV acceleration voltage and 7–11 spot size under high vacuum. EDS measurements were taken with 10 kV acceleration voltage having a 50,000 × magnification with a working distance of 10 mm. The transmission change with respect to wavelength was determined by Jasco/V-750 UV/VIS Spectrophotometer.

3 Results and discussion

The top view morphologies of $Sb_2(S_xSe_{1-x})_3$ thin films with different S/S + Se ratios (Fig. 1a–e) were examined using scanning electron microscopy (SEM). The Sb_2Se_3 precursor layer composed of closely distributed small grains with a grain size of ~ 100 nm as shown in Fig. 1a. The morphology of the precursor layer was seemed to change dramatically after sulfurization. For the film with $x = 0.12$, SEM images showed that the grain size of the film got bigger as the sulfur introduced into the system, confirming prior findings that larger Sb_2S_3 grains were generated at this temperature than Sb_2Se_3 [29]. As it can be seen in Fig. 1b, grains with diameter of several hundred nanometers were formed on the sample surface and the distribution of the $Sb_2(S_xSe_{1-x})_3$ grains was compact. Moreover, there were no distinct pinholes on the sample surface. When the S content of the $Sb_2(S_xSe_{1-x})_3$ thin films increased to $x = 0.35$ (Fig. 1c), pinholes started to form in the film, which could be due to higher volume shrinkage when more Se was substituted by S in the film. Large $Sb_2(S_xSe_{1-x})_3$ grains can no longer be observed in some areas of the sample surface. When the sulfur content was increased more (Fig. 1d), number of small grains increased and several tens of nanometer pinholes appeared all over the surface, suggesting severe decomposition of the $Sb_2(S_xSe_{1-x})_3$ thin films due to high sulfur vapor pressure during sulfurization. Notably, the SEM image of the $Sb_2(S_xSe_{1-x})_3$ film with $x = 0.12$ showed some round grains which implies that grains start to grow in the vertical direction. For films with higher sulfur concentrations, grains seemed to grow in a horizontal direction as verified by XRD analysis.

EDS was employed to examine the chemical compositions of fabricated $Sb_2(S_xSe_{1-x})_3$ thin films. According to EDS analysis of these films (Table 1), $Sb_2(S_xSe_{1-x})_3$ thin films were successfully synthesized with the sulfur contents of $x = 0$, 0.12, 0.35, 0.48 and 0.86 utilizing various sulfur loadings of 0, 1, 2, 3 and 4 mg, respectively, during the annealing. Apparently, the films with higher sulfur content were obtained as increasing the amounts of sulfur powder employed during the annealing process.

Figure 2 shows the X-ray diffraction patterns of $Sb_2(S_xSe_{1-x})_3$ thin films with different S/S + Se ratios. All films showed polycrystalline structure and exhibited characteristic peaks of $Sb_2(S_xSe_{1-x})_3$ thin films. Moreover, there were no peaks corresponding to any impurity or secondary phases in our samples, showing that they are single-phase. The film with $x = 0$ exhibited diffraction peaks along (020), (120), (101), (230), (211), (221), (301), (240) and (440) crystallographic planes at 2θ values of 14.93, 16.75, 23.80, 27.28, 28.10, 31.08, 32.12, 34.00 and 43.92°, respectively. Typically, XRD pattern of the film with $x = 0$ matched well with the orthorhombic Sb_2Se_3 (JCPDS no. 15–0861) and showed preferential orientation along (020) plane. As the sulfur was introduced to the system, the XRD patterns clearly represented the fluctuation of the S/(S + Se) ratio in the $Sb_2(S_xSe_{1-x})_3$ thin films. With increasing S content in the films, the diffraction peaks progressively shifted towards larger angles. The peak shift in the XRD is based on the dopant size. Considering that sulfur atoms (1.84 Å) is smaller than selenium atoms (1.98 Å), lattice constants would decrease when S substitutes for Se sublattice of $Sb_2(S_xSe_{1-x})_3$. This leads to smaller interplanar spacing and 2θ shifts to higher values according to Bragg's law. In the

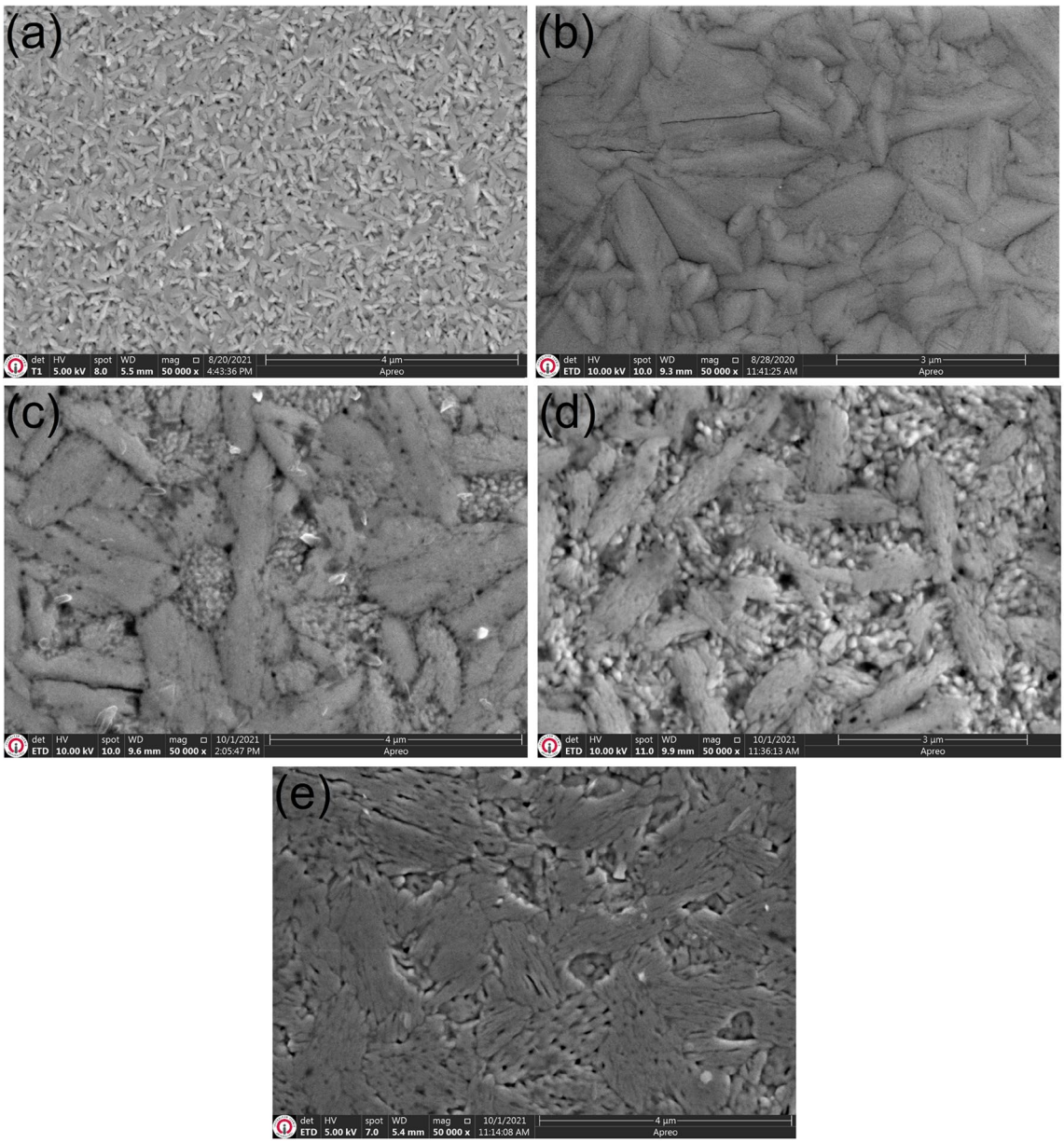

Fig. 1 SEM images of $Sb_2(S_xSe_{1-x})_3$ thin films with sulfur contents of **a** $x=0$, **b** $x=0.12$, **c** $x=0.35$, **d** $x=0.48$ and **e** $x=0.86$

Table 1 Average atomic compositions of fabricated $Sb_2(S_xSe_{1-x})_3$ thin films

	[Sulfur] mg	[Sb] atomic %	[Se] atomic %	[S] atomic %	[x] S/(Se + S)	Sb/(Se + S)
Sample 1	0	43.70	56.30	0.00	0.00	0.78
Sample 2	1	41.07	52.14	6.79	0.12	0.70
Sample 3	2	42.23	37.39	20.38	0.35	0.73
Sample 4	3	42.39	30.21	27.69	0.48	0.73
Sample 5	4	42.67	8.30	49.03	0.86	0.74

case of, $x=0.86$ sample, since more S substitutes for Se sublattice, this shift is more apparent.

As can be seen from Fig. 2, the intensity of the diffraction peaks increases as the sulfur concentration of the films increases from $x=0$ to $x=0.35$, indicating improvement of

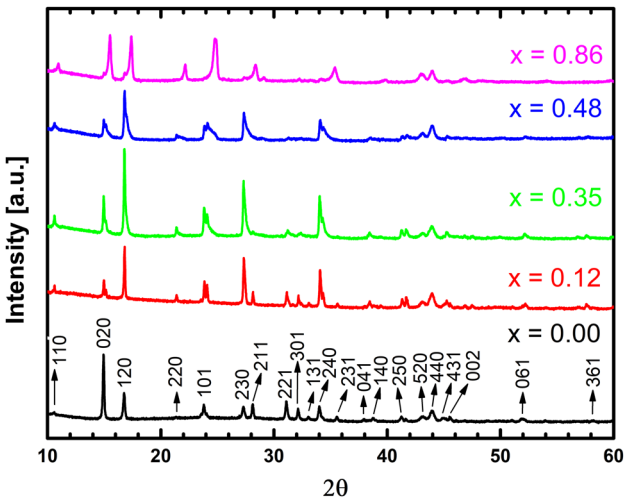

Fig. 2 XRD spectra of $Sb_2(S_xSe_{1-x})_3$ thin films with the sulfur contents of $x=0$, 0.12, 0.35, 0.48 and 0.86

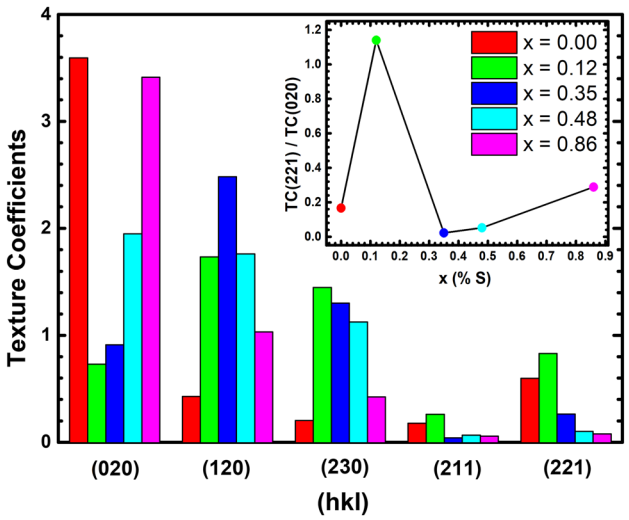

Fig. 3 The texture coefficients (TC) of the diffraction patterns of the $Sb_2(S_xSe_{1-x})_3$ thin films. (Inset graph: variation of the TC (221)/TC (020) ratio of the diffraction patterns.)

crystallinity for these samples. While the preferred orientation is (020) for the film with $x=0$, it is put in place to the (120) plane for the films with $x=0.12$ and $x=0.35$. When the sulfur concentration is increased to 0.48, the intensity of the peaks decreases with the change of preferred orientation from (120) to (020), which reveals the reduction in crystallinity. Deterioration of crystallinity suggests decomposition of the $Sb_2(S_xSe_{1-x})_3$ thin films due to high sulfur vapor pressure during sulfurization as verified by SEM analysis. Change in preferred orientation of the films is related to their lowest overall energy. There are two possible mechanisms that are believed to affect the crystal orientations. They are nucleation and final growth. The initial orientation is favored on the surface, with the nuclei tending to develop a minimal free energy configuration. Ultimate growth orientation results from the survival of nuclei with an energetically unstable plane parallel to the surface of the substrate among randomly oriented nuclei due to their different growth rates. This means that the growth orientation is developed to a crystallographic direction of the lowest surface energy. Then, the grains grow larger as long as the film grows with a lower surface energy density. Our results suggest that sulfur vapor pressure during sulfurization seriously affect the crystallinity and preferred orientation of the $Sb_2(S_xSe_{1-x})_3$ thin films.

The crystal orientation of the $Sb_2(S_xSe_{1-x})_3$ thin films is an important factor in determining the solar cell's performance since it provides important information about charge carrier transfer and the formation of useful grain boundaries [10]. $Sb_2(S_xSe_{1-x})_3$ films can crystallize in either horizontal (*hkl*, $l=0$) or vertical (*hkl*, $l\neq0$) orientations during deposition, depending on the substrate type and temperature. Vertical crystallization in which c-axis bends to the substrate is thought to be advantageous for charge carrier transport along the absorber layer in photovoltaic applications [30, 31]. The intensity of (*hk*0) planes of (020), (120), and (230) was greater in comparison to (*hkl*) planes of (211) and (221), as seen in the XRD patterns of fabricated $Sb_2(S_xSe_{1-x})_3$ films (Fig. 2).

The texture coefficient (TC) of diffraction patterns of the samples sulfurized under varied sulfur concentrations were calculated to assess the difference in preferential orientations using the following equation [32]:

$$TC_{hkl} = \frac{I_{hkl}}{I_{0hkl}} \Big/ \left(\frac{1}{N} \sum_{N} \frac{I_{hkl}}{I_{hkl}} \right) \quad (1)$$

where $I_{(hkl)}$ is the measured peak intensity of the (*hkl*) plane, $I_{0(hkl)}$ is the peak intensity in the standard XRD pattern (JCPDS: 15–0861), and N is the total number of reflections considered for the calculation. The preferential orientation along a specific plane of the film is indicated by a higher TC value for specific diffraction peaks. As it can be seen in Fig. 3, the (*hk*0) planes had a greater TC value than the (*hk*1) planes for the fabricated $Sb_2(S_xSe_{1-x})_3$ films. This demonstrated that the (*hk*0) planes in $Sb_2(S_xSe_{1-x})_3$ thin films were highly textured in general and growth was orientated along [*hk*0]. On the other hand, as the *S* content in the films increased from 0 to 0.12, the TC of (*hk*1) orientation increases as in (211) and (221). When the TCs of the two typical crystal planes, (221) and (020) were compared (in inset graph of Fig. 3), it was observed that TC (221)/TC (020) ratio increases with the addition of small amount of sulfur ($x=0.12$). However, as the sulfur amount in the films increased more, TC (221)/TC (020) ratio seriously

decreased. This finding was further verified by SEM surface analysis, which showed that high grain size and flat surface morphology having more grains in the vertical direction for the $Sb_2(S_xSe_{1-x})_3$ thin film with $x=0.12$. To sum up, sulfurization of Sb_2Se_3 had a critical role in orientation, as evidenced by the difference in these results. The sample with a sulfur content of 0.12 can be considered optimum because the $Sb_2(S_xSe_{1-x})_3$ thin films with (*hk*1) orientations perform well in carrier transport [31].

The optical bandgaps of the $Sb_2(S_xSe_{1-x})_3$ thin films were determined by measuring their transmission spectra in the wavelength range of 600–1100 nm. The transmission spectra of the $Sb_2(S_xSe_{1-x})_3$ thin films showed a blue shift toward shorter wavelengths as the S content in the films increases as illustrated in the inset of Fig. 4, relating to widened bandgaps of the films. Optical bandgaps of the $Sb_2(S_xSe_{1-x})_3$ thin films were calculated from the formula $\alpha h\nu = A\left(h\nu - E_g\right)^{1/2}$ [33]. Bandgaps of the films were deduced from the extrapolation of the linear plots of $(\alpha h\upsilon)^2$ versus $(h\upsilon)$. The optical bandgaps of the $Sb_2(S_xSe_{1-x})_3$ thin films were determined as 1.25 eV, 1.30 eV, 1.33 eV, 1.38 eV and 1.43 eV for $x=0$, 1, $x=0.12$, $x=0.35$, $x=0.48$ and $x=0.86$, respectively. Optical, characterizations of the fabricated thin films revealed that $Sb_2(S_xSe_{1-x})_3$ thin films with suitable bandgap can be obtained by the adjustment of the S/S + Se atomic ratio.

Raman scattering was used to further explore the structure of $Sb_2(S_xSe_{1-x})_3$ thin films sulfurized with different sulfur contents. It is known that Sb_2S_3 is isostructural to Sb_2Se_3 and both compounds have a comparable Pnma phase. The Raman vibrational mode assignment of these compounds is nearly same, and both has 30 Raman active modes [34]. As specified in the following equation, Raman active optical modes at the Γ point of the Brillouin zone is represented as follows [35]:

$$\Gamma = 10\mathrm{Ag} + 5\mathrm{B1g} + 10\mathrm{B2g} + 5\mathrm{B3g} \quad (2)$$

However, only a few numbers of them have been detected experimentally [13]. Figure 5 shows the Raman spectrum of the fabricated samples. The vibrational modes of 144, 188, and 252 cm^{-1} were seen in all $Sb_2(S_xSe_{1-x})_3$ thin films, confirming that the basic lattice structure was preserved in the fabricated samples, and the peaks for $Sb_2(S_xSe_{1-x})_3$ thin films matched well with previous studies [36]. In the Raman spectrum of pure Sb_2Se_3, Sb–Se vibration modes with characteristic peaks found at wavenumbers of 188 and 210 cm^{-1} were referred to as A1g Raman modes [13, 36]. At 252 cm^{-1}, additional characteristic peak of the A1g Raman active mode of Sb_2Se_3 was detected because of Se–Se stretching vibrational bonds [37, 38]. Another peak at around 144 cm^{-1} shows antimony metal signals in the Sb_2Se_3 thin film [35]. As the sulfur was introduced to the system, weak vibrational modes at 310 cm^{-1} arise, and its intensity increased as the S concentration of the films increased. The peak at the wavenumber of 280 cm^{-1} was also visible for the film with $x=0.86$. Vibrational modes at 280 cm^{-1} and 310 cm^{-1} can be correlated to Ag and B1g vibrational modes of Sb_2S_3, respectively [39]. Peak found at the wavenumber of 188 cm^{-1} was attributed to Ag modes of Sb_2S_3 [39].

In comparison to the $Sb_2(S_xSe_{1-x})_3$ thin film with $x=0.12$, the peak intensities were smaller for the other samples (Fig. 5). Because of the optical transition selection principles, the Raman signal is affected by crystal orientations. As a result, when the grains are oriented randomly, the

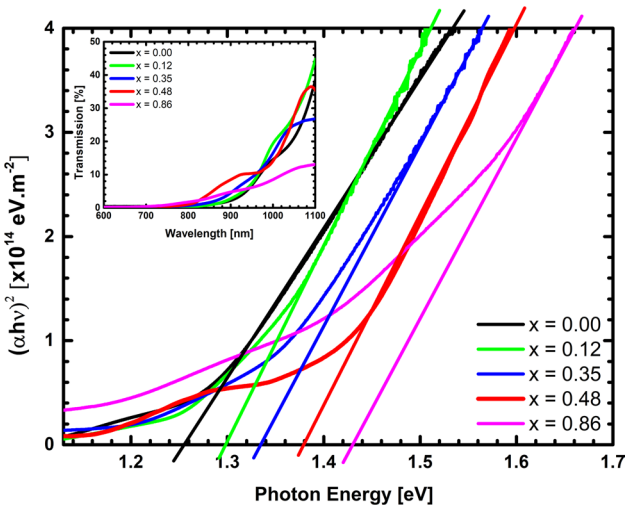

Fig. 4 Optical bandgap energy of $Sb_2(S_xSe_{1-x})_3$ thin films with the sulfur contents of x = 0, 0.12, 0.35, 0.48 and 0.86. (Inset graph: transmission spectra of $Sb_2(S_xSe_{1-x})_3$ thin films)

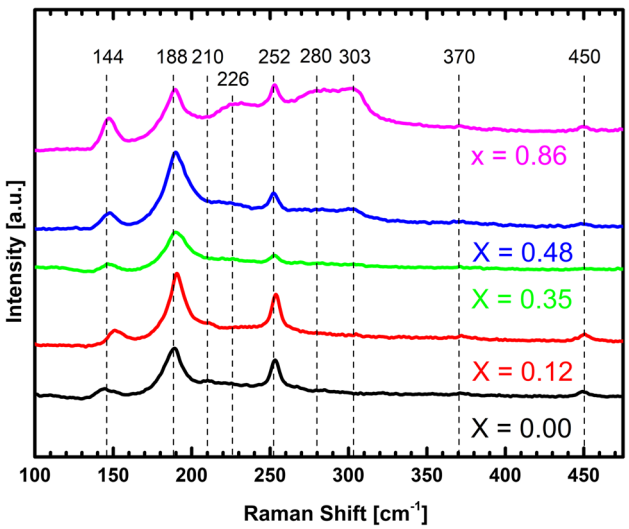

Fig. 5 Raman spectrum of $Sb_2(S_xSe_{1-x})_3$ thin films with the sulfur contents of $x=0$, 0.12, 0.35, 0.48 and 0.86

scattering intensity ratios can be significantly influenced [40]. The grains in the $Sb_2(S_xSe_{1-x})_3$ thin films with $x=0.35$ and 0.48 had a broad size distribution, and arbitrarily oriented crystal formation was common as it can be seen in SEM images, which may have led to reduced Raman peak intensities in these samples. Overall, there is no discernible trend in peak intensities when shifting from composition $x=0$ to composition $x=1$. Moreover, films with $x>0.12$ have broader bands in the scattering volume which can be indication of by structural defects or a change in the composition of the films. This finding was further verified by SEM surface analysis, which showed pinhole development for these films.

In Fig. 5, Raman spectra of $Sb_2(S_xSe_{1-x})_3$ thin films contain two additional peaks at 370 and 450 cm^{-1}, indicating undesired secondary phase formation of Sb_2O_3 [38]. In the XRD analysis shown in Fig. 2, however, no oxide phase of $Sb_2(S_xSe_{1-x})_3$ films was identified. The laser heating impact of the Raman setup may have caused the creation of the oxide phase. Applied laser power during Raman investigations in an ambient air causes S and Se to evaporate off the sample surface due to their high vapor pressure. Sb_2O_3 may have been generated because of S and Se being replaced by oxygen from the air during this process [38].

4 Conclusions

In summary, $Sb_2(S_xSe_{1-x})_3$ thin films with $x=0$, 0.12, 0.35, 0.48 and 0.86 were fabricated by sulfurization of magnetron sputtered Sb_2Se_3 thin films using sulfur powder as the sulfur source. Optical, morphological, and structural characterizations of the fabricated $Sb_2(S_xSe_{1-x})_3$ thin films revealed that, $Sb_2(S_xSe_{1-x})_3$ thin films with suitable bandgap, favorable orientation and compact morphology can be obtained by the adjustment of the S/S + Se atomic ratio. Among the $Sb_2(S_xSe_{1-x})_3$ thin films fabricated by the present two-step method, the film with $x=0.12$ displayed compact morphology with grains having diameter of several hundred nanometers. Moreover, its optical gap of 1.30 eV can be considered optimum according to the Shockley–Queisser model. Moreover, it was observed that TC of [*hk*1] direction was higher for the film with $x=0.12$ which is important for carrier transport. However, for the $Sb_2(S_xSe_{1-x})_3$ thin films having x higher than 0.12, it was observed that growth was more orientated at [*hk*0] direction. Furthermore, pinholes started to form in the final films for high *x* values, which could be due to higher volume shrinkage when more Se was substituted by S in the $Sb_2(S_xSe_{1-x})_3$ thin films.

Acknowledgements This research was supported by The Scientific and Technological Research Council of Turkey (TUBITAK) with the Project No. of 118F143. The authors would like to acknowledge the facilities of Research and Application Center for Quantum Technologies (RACQUT) and ISTE Center for Science and Technology Studies and Research (ISTE-CSTSR) for the current study.

References

1. M.A. Green et al., Prog in photovoltaics **26**(1), 3–12 (2018)
2. S. Frontier, Solar Frontier achieves world record thin-film solar cell efficiency of 22.9%. News Item 20 (2017)
3. A. Cantas et al., J Phys D: Appl Phys **51**(27), 275501 (2018)
4. D.G. Buldu et al., Phys. Scr. **93**(2), 024002 (2018)
5. S. Kim, J.S. Park, A. Walsh, ACS Energy Lett. **3**(2), 496–500 (2018)
6. T. Ratz et al., J Phys Energy **1**(4), 042003 (2019)
7. F. Turkoglu et al., Thin Solid Films **670**, 6–16 (2019)
8. A. Mavlonov et al., Sol Energy **201**, 227–246 (2020)
9. C. Chen et al., Appl Phys Lett **107**(4), 043905 (2015)
10. X. Wen et al., Nat Commun **9**(1), 1–10 (2018)
11. Z. Li et al., Nat. Commun **10**(1), 1–9 (2019)
12. W. Shockley, H.J. Queisser, J Appl Phys **32**(3), 510–519 (1961)
13. B. Yang, J. Tang et al., Sci. Rep. **5**(1), 11 (2015)
14. Y.C. Choi et al., Adv Energy Mater **4**(7), 1301680 (2014)
15. K. Li et al., Solar RRL **4**(9), 2000220 (2020)
16. X. Wang et al., Adv Energy Mater **10**(40), 2002341 (2020)
17. H. Lei, J. Chen, Z. Tan, G. Fang, Solar RRL **3**(6), 1900026 (2019)
18. E.A. El-Sayad, J Non Cryst Solids **354**(32), 3806–3811 (2008)
19. A. Polman et al., Science **352**(6283), 307 (2016)
20. C.L. McCarthy, D.H. Webber, E.C. Schueller, R.L. Brutchey, Angew. Chem. **127**(29), 8498–8501 (2015)
21. O.A. Jaramillo-Quintero, M.E. Rincón, G. Vásquez-García, P.K. Nair, Prog. Photovolt: Res Appl **26**(9), 709–717 (2018)
22. C. Wu et al., Sol Energy Mater Sol Cells **183**, 52–58 (2018)
23. C. Wu et al., ACS Appl Mater Interfaces **11**(3), 3207–3213 (2018)
24. Y. Zhang et al., Solar RRL **1**(5), 1700017 (2017)
25. W. Wang et al., Adv Electron Mater **5**(2), 1800683 (2019)
26. C. Jiang et al., Cell Reports Physical Science **1**(1), 100001 (2020)
27. F. Turkoglu et al., J Appl Phys **123**(16), 165104 (2018)
28. Y. Demirhan et al., Renew Energy **146**, 1549–1559 (2020)
29. S. Yuan et al., Sol Energy Mater Sol Cells **157**, 887–893 (2016)
30. R. Kondrotas, J. Zhang, C. Wang, J. Tang, Sol Energy Mater Sol Cells **199**, 16–23 (2019)
31. Z. Li et al., Sol Energy Mater Sol Cells **161**, 190–196 (2017)
32. G.B. Harris, Lond. Edinb. Dublin Philos. Mag. J. Sci. **43**(336), 113–123 (1952)
33. H. Deng et al., Prog. Photovolt: Res Appl **26**(4), 281–290 (2018)
34. I. Efthimiopoulos et al., Sci. Rep. **3**, 2665 (2013)
35. Y, Liu, K.T.E. Chua, T.C. Sum, C.K. Gan, Phys. Chem. Chem. Phys. **16**(1), 345–350 (2014)
36. M.D. Khan, S.U. Awan, C. Zequine, C. Zhang, R.K. Gupta, N. Revaprasadu, ACS Applied Energy Materials **3**(2), 1448–1460 (2020)
37. J. Tao, J. Chu et al., Sol. Energy Mater. Sol. Cells **197**(1), 6 (2019)
38. A. Shongalova et al., MRS Commun. **8**(3), 865–870 (2018)
39. C.J. Diliegros-Godines, J.S. Cruz, N.R. Mathews, M. Pal, J Mater Sci **53**(16), 11562–11573 (2018)
40. W. Farfán, E. Mosquera, C. Marin, Adv Sci Lett **4**(1), 85–88 (2011)